

Learning Dynamic View Synthesis With Few RGBD Cameras

Shengze Wang¹, YoungJoong Kwon¹, Yuan Shen², Qian Zhang¹, Andrei State¹, Jia-Bin Huang^{1,3}, and Henry Fuchs¹

¹ UNC-Chapel Hill

² UIUC

³ Virginia Tech

Abstract. There have been significant advancements in dynamic novel view synthesis in recent years. However, current deep learning models often require (1) prior models (e.g., SMPL human models), (2) heavy pre-processing, or (3) per-scene optimization. We propose to utilize RGBD cameras to remove these limitations and synthesize free-viewpoint videos of dynamic indoor scenes. We generate feature point clouds from RGBD frames and then render them into free-viewpoint videos via a neural renderer. However, the inaccurate, unstable, and incomplete depth measurements induce severe distortions, flickering, and ghosting artifacts. We enforce spatial-temporal consistency via the proposed Cycle Reconstruction Consistency and Temporal Stabilization module to reduce these artifacts. We introduce a simple Regional Depth-Inpainting module that adaptively inpaints missing depth values to render complete novel views. Additionally, we present a Human-Things Interactions dataset to validate our approach and facilitate future research. The dataset consists of 43 multi-view RGBD video sequences of everyday activities, capturing complex interactions between human subjects and their surroundings. Experiments on the HTI dataset show that our method outperforms the baseline per-frame image fidelity and spatial-temporal consistency. We will release our code, and the dataset on the website soon.

Keywords: Novel View Synthesis, Datasets

1 Introduction

Dynamic novel view synthesis is the task of using a set of input video frames to synthesize videos of the dynamic scene from novel viewpoints. High-quality dynamic novel view synthesis could benefit applications such as virtual tourism, 3D photography, virtual avatars, and telepresence. In this work, we are interested in capturing the interaction between human and their surroundings via dynamic novel view synthesis for indoor scenes. There have been significant advances in dynamic novel view synthesis in recent years. However, much of the recent work [22,15,36] on general dynamic novel view synthesis is not *generalizable* (i.e., they require test-time per-video optimization). Other work [24,38,21,50,33] relies on

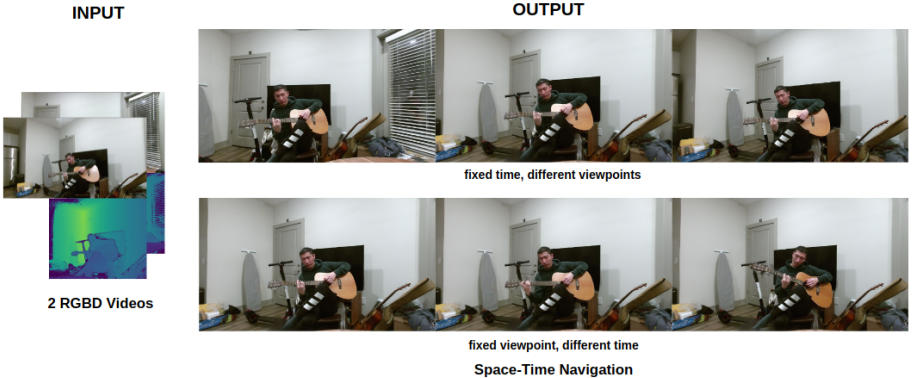


Fig. 1. We use two RGBD videos to generate free-viewpoint videos for dynamic indoor scenes. The above shows synthesized novel views for an evaluation sequence. Our approach generalizes to new people, actions, objects, and environments without per-scene optimization, prior models of objects, or expensive preprocessing.

object-specific priors (e.g., SMPL[25], STAR[34]) to adapt to new dynamics of the object. The underlying reason is that this prior art often uses monocular videos as inputs, which lacks the epipolar constraints required to resolve ambiguities in registration and matching. We leverage a sparse set of commodity RGBD cameras to resolve this ambiguity. LookinGood[28] and HVSNet[33] are thus closely related to our approach. They both utilize RGBD camera inputs, and they achieve great visual qualities while being able to generalize to new people and actions. However, neither work showed generalization to the entire dynamic scenes. HVSNet[33] utilized synthetic datasets to learn to generalize to new human subjects. However, it is difficult to create synthetic data that faithfully captures the interactions between humans and objects. Thus, it is a non-trivial task to learn to generalize to human-object interactions with synthetic data. On the other hand, LookinGood[28] achieves such generalization using colored dynamic human models generated by non-rigid reconstructions techniques like [32,14,6,65,9]. In this work, we try to remove the dependency on heavy preprocessing and learn to directly perform dynamic novel view synthesis from raw RGBD data.

Depth estimation is a core component in novel view synthesis. Much prior art [29,62,35,22,15] regresses the scene geometry for each video test-time, which takes significant time and prevents generalizing to new scenes. On the other hand, publicly available commodity RGBD cameras (e.g. Microsoft Kinect) provide instant measurements of the scene geometry. They thus present the possibility of simplifying the task of geometry estimation for novel view synthesis. Therefore, we utilize a sparse set of stationary RGBD cameras in our approach to avoid per-video optimization. With the access to multi-view RGBD video observations at any frame, one could use existing static novel view synthesis models [41,42]

to generate novel view images for each frame separately and later combine the novel view images into a free-viewpoint video of the dynamic scene. However, the unstable, inaccurate, and incomplete depth measurements lead to significant spatial and temporal inconsistencies. As a result, the synthesized free-viewpoint videos often have significant distortion, flickering, and ghosting artifacts. To reduce these artifacts, we propose to explicitly enforce spatial-temporal consistency in the model. We introduce the Cycle Reconstruction Consistency to enforce consistency between the synthesized novel views and the input views. We improve the temporal consistency via a Temporal Stabilization module that utilizes temporal information to stabilize the video synthesis process and generate more consistent and complete novel view videos. Finally, to synthesize novel views that are complete despite the incomplete depth measurements, we introduce a simple Regional Depth-Inpainting module that adaptively performs local depth-inpainting based on surrounding valid depth measurements. We show in our evaluation that each of the proposed components provides solid improvements to the synthesized novel views.

The training process also poses significant challenges due to the lack of dynamic multi-view RGBD datasets. Most prior multi-view RGBD datasets either contain only static scenes [48,31] or overly simplistic environments [19], or they are no longer available [55]. Therefore, to facilitate the training of dynamic novel view synthesis, we captured a new dynamic multi-view RGBD dataset, the Human-Things Interaction (HTI) dataset, to capture the complex interactions between one or more human subjects and objects in different environments. To summarize, our contribution are:

- We introduce an approach for dynamic novel view synthesis based on a sparse set of stationary commodity RGBD cameras. Our system can generalize to new actions, objects, people, and environments without per-scene optimization, prior knowledge of the scene, or heavy preprocessing steps.
- We propose Cycle Reconstruction Consistency and Temporal Stabilization modules to enforce spatial-temporal consistency. Our approach notably reduces distortions, flickering, and ghosting artifacts in the synthesized free-viewpoint videos. We also introduce a simple Regional Depth-Inpainting module that helps generate complete novel view images from incomplete depth measurements.
- We introduce a new multi-view RGBD dataset, the Human-Things Interaction (HTI), to facilitate learning dynamic novel view synthesis. It captures complex interactions between people and their environments. The dataset consists of 43 multi-view RGBD videos and 77,529 frames of various people interacting with other people or objects in 7 different environments captured from 12 different setups. Our code and the HTI dataset will be made public upon publication.

2 Related Work

2.1 Static Novel View Synthesis

Layered Representations. Existing methods differ in the way that they represent the 3D scenes. Multiplane Image(MPI) representation [51,64,49,54,4,8] achieves free-viewpoint movement by capturing the scene with a set of fronto-parallel planes, layered-meshes, or multilayer-spheres. However, these methods usually have a limited range of movement for novel viewpoints to move and exhibit the stack-of-card artifacts when large motions exist in the novel viewpoints.

Neural Radiance Fields. Neural radiance fields (NeRF) [29] introduced a simple but powerful architecture based on Multi-Layer Perceptrons (MLPs) and differentiable volumetric rendering. It achieves unprecedented photorealism for novel view synthesis and supports a large range of movements for novel viewpoints. The high-level idea is to use an MLP to model the volumetric neural radiance field of the target scene. The utilization of positional encodings plays a vital role in improving the sharpness and fidelity of the reconstructed radiance field. Lots of following works [62,5,52,47,56,10] have been built upon the NeRF, and NeRF-based methods are currently the state-of-the-art methods in terms of photorealism. However, NeRF-based methods have three main limitations: 1) slow training and rendering speed. To address this issue, some work [23,30,60,1,17,16,13] has been proposed to improve upon this problem. 2) inability to encode dynamic scenes. Works like [58,22,35,36] has been proposed to encode dynamic scenes. 3) inability to generalize to new scenes. While many works like [61,10,56,12] have tried to encode prior knowledge about the world into the model via CNNs or Transformers to achieve generalizability, it still remains a challenge to learn generalizable neural radiance fields.

Explicit 3D Representations. One of the fundamental difficulties in novel view synthesis is the task of estimating the 3D geometries of the scene from input images. To alleviate the burden from the view synthesis models, recent works [41,42,20,44,2] rely on preprocessed raw 3D geometries, e.g., point clouds or meshes, obtained from multi-view stereo software such as COLMAP[45]. Leveraging the explicit geometry, they can be less prone to fog-like artifacts, as seen in NeRF-based methods. Methods like [41,42] also demonstrate generalizability to new scenes. Point cloud-based neural rendering approaches [20,44,57] show strength in encoding large-scale scenes and thin structures as well as preserving sharpness and details. However, their synthesis quality heavily depends on the accuracy and completeness of the preprocessed 3D representations.

2.2 Dynamic Novel View Synthesis

Dynamic Novel View Synthesis of General Scenes Dynamic novel view synthesis is the task of performing novel view synthesis for dynamic scenes. It is more challenging than static novel view synthesis due to the moving objects, deforming surfaces, occlusion, and changing topologies. Many of the prior arts [58,22,15,53] intend to generate 3D videos from monocular videos by encoding

the dynamic scene as spatial-temporal neural radiance fields. They often learn a radiance field along with a warping field. The warping field warps the static radiance field to conform to the monocular video input. Optical flow and monocular depth estimators are often used to guide the optimization to a good local optimum. They also benefit from applying constraints on the smoothness of spatial movements, color consistencies for static and dynamic content, etc. However, due to the inherent ambiguities in monocular captures of dynamic scenes, it is common to observe blurry and fog-like artifacts in these methods. Similar to static NeRF-based methods, these approaches require per-video optimization and cannot generalize to new scenes. Moreover, it is challenging to apply these kinds of methods to long videos [22,15]. TöRF[3] enables effective utilizations of time-of-flight sensors for both static and dynamic scenes. For dynamic scenes, TöRF builds upon NSFF. In this work, we present a dynamic novel view synthesis approach that does not require per-video optimization and is not limited by the length of the video. The work by Yoon et al.[59] is most related to our work. They utilize multi-view stereo and monocular depth estimators to estimate spatially and temporally coherent depth maps and scene flow fields. They use the depth, maps, and scene flow fields to generate novel view videos of dynamic scenes. Their approach does not require per-video optimization or prior knowledge of the scene.

Human-Specific Dynamic Novel View Synthesis. Recent works [38,24,50,37] often use colored videos as inputs and focus on animating clothed humans. These approaches leverage human body templates, e.g., SMPL[25] and STAR[34], and deep-textures and generalize to the unseen poses. Nonetheless, they cannot generalize to previously unseen subjects. Kwon *et al.* [21] achieves generalization to arbitrary human subjects by anchoring the pixel-aligned features on the SMPL model. On the other hand, several approaches have utilized color and depth inputs. LookinGood[28] utilized 16 IR cameras to provide depth measurements and 8 color cameras to capture the appearance. They utilize a non-rigid reconstruction pipeline similar to Motion2Fusion[14] to perform real-time reconstruction of the human subject. They re-render the colored mesh to generate high-quality novel views, and their approach can generalize to new people and actions. Their approach can likely generalize to the entire environment and capture interactions between humans and objects. However, our work focuses on achieving dynamic novel view synthesis using raw color and depth inputs from sparse commodity RGBD cameras without heavy preprocessing. Moreover, the non-rigid reconstructions are inherently more stable than the raw RGBD inputs we are using. As a result, we face more challenges in generating temporally consistent novel view videos. HVSNet [33] can synthesize novel views of moving human subjects using monocular RGBD captures. It renders novel views from a feature point cloud of the person and enhances the point cloud with pose-aligned human models. They trained their model on a large-scale synthetic dataset of dynamic 3D human models and then evaluated on real-world captures from the 3dMD scanner system. Our work focuses on using commodity RGBD cameras to synthesize novel views of the entire dynamic scene, including the interactions be-

tween humans and their surroundings. It is difficult to create synthetic datasets that synthesize such interactions faithfully. As a result, learning to generalize through synthetic data is challenging in our scenario.

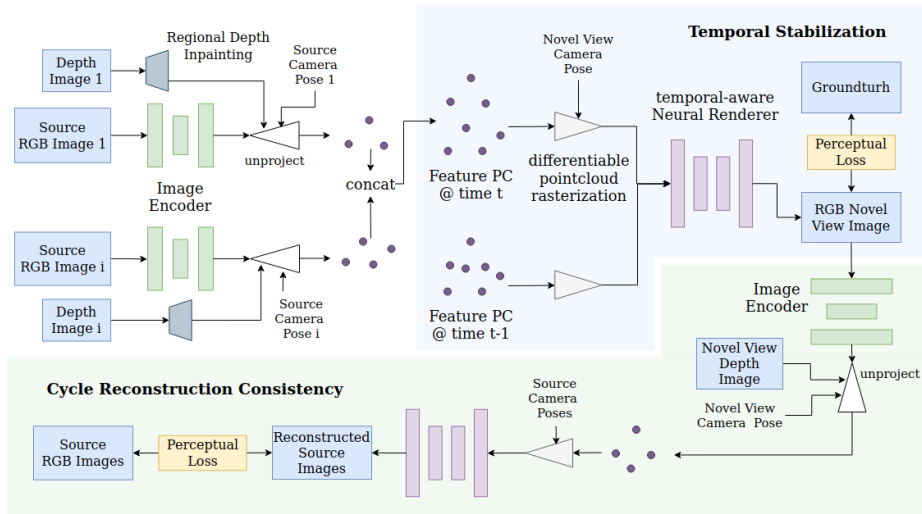


Fig. 2. Overview of our system. Set of source a shared image encoder encodes RGB images. The resulting 2D features are lifted into 3D feature point clouds leveraging the depth map refined by the depth inpainting module. The point clouds are then rasterized and synthesized by a neural renderer into a novel view image. The output image is supervised with the perceptual and proposed Cycle Reconstruction Consistency.

3 Method

Given the synchronized and calibrated multi-view RGBD videos, our method renders a novel view video of an arbitrary dynamic scene (Fig. 1). We aim to synthesize realistic, complete, and spatial-temporally consistent novel views. The system pipeline is shown in Fig. 2. Our method follows common approaches to synthesizing novel views from feature point clouds generated from the RGBD input. First, we complete the raw depth maps from RGBD cameras via our proposed Regional Depth-Inpainting module. To reduce distortion, flickering, and ghosting artifacts in the rendered novel view video, we enforce spatial-temporal consistency of the synthesized novel views via a new Cycle Reconstruction Consistency and Temporal Stabilization based on a temporal-aware neural renderer. Mathematically, given a set of color images I , their corresponding depth images D and poses C , and a novel viewpoint C_{nv} , our model Φ synthesizes the novel view image I_{nv} at C_{nv} :

$$I_{nv} = \Phi(D, I, C, C_{nv}). \quad (1)$$

3.1 Feature Point Cloud and Neural Rendering

We follow standard convention for neural rendering from feature point clouds [40]. Given the RGB image $I_{src,i}$ of size $H \times W \times 3$ from the i th view, we first extract a feature map $F_{src,i} \in \mathbb{R}^{H \times W \times M}$, where M is the feature dimension. We then lift the 2D pixels into a point cloud $P_{src,i}$ by assigning each pixel $x_{src} = [u, v, 1]^T$ a 3D point position $p_{src,i}$ using its corresponding depth measurement $d_{src,i}$ in the depth map $D_{src,i}$. Mathematically, this process can be expressed as:

$$p_{nv,i} = R_{src2nv,i} \cdot (d_{src,i} \cdot K_{src,i}^{-1} \cdot x_{src,i}) + t_{src2nv,i}, \quad (2)$$

where $K_{src,i} \in \mathbb{R}^{3 \times 3}$ is the intrinsic parameter of the i th source camera. $R_{src2nv,i}$ and translation $t_{src2nv,i}$ transform the point clouds into the frame of the novel view camera C_{nv} . We concatenate all point clouds into a global point cloud P_{nv} . Next, we differentially rasterize the feature point cloud into the projected feature map F_{nv} with Pytorch3D[40]. We then use a U-Net [43] based network as the neural renderer to decode the projected feature map F_{nv} into an RGB novel view image I_{nv} .

3.2 Baseline Loss Function

Given the ground truth image I_{gt} at the novel viewpoint C_{gt} and the synthesized novel view image I_{nv} , we use the perceptual loss proposed by Chen and Koltun [11] as the baseline loss function. The loss function is described as follows:

$$L(I_{nv}, I_{gt}) = \|I_{nv} - I_{gt}\|_1 + \sum_l \lambda_l \|\phi_l(I_{nv}) - \phi_l(I_{gt})\|_1, \quad (3)$$

where ϕ is a pretrained VGG-19 network [46], ϕ_l is the output feature map of the l th layer of the network and $l \in [1, 5]$. λ_l are the weights of the loss calculated for layer l as defined in [11].

3.3 Regional Depth-Inpainting

Raw depth maps are often not enough to generate high-fidelity complete novel views. They are often incomplete due to limited ranges and fields of view (FOV) of depth sensors, highly slanted smooth surfaces, etc. This incompleteness leads to holes in point clouds and missing regions in the reprojected feature maps, and thus blobs of artifacts as shown in Fig. 4. Therefore, we utilize a monocular depth estimator (e.g. MiDaS[39]) to complete the depth maps.

A naive way is to find a least-squares alignment from the estimated depth map to the raw depth map. However, this usually leads to bad results because the estimated depth map is often inaccurate. We notice that local patches of the estimated depth maps usually have gradients close to the gradients in the raw depth map patch. Therefore, we propose to perform regional depth alignments.

We first fuse the depth maps from all source cameras into a global point cloud. The point cloud is then rendered as depth map D_{raw} for the source camera of

interest. Next, we generate a mask U to flag the missing values in the depth image D_{raw} . We then perform morphological filtering (closing then opening) on U to create large connected regions, where most pixels have no depth values. We then label these regions with numbers. We also estimate a depth map D_{mono} for the source image.

Given a region g in mask U , we expand it to include a set of pixels with valid depth values in both D_{raw} and D_{mono} . For these pixels, we denote their depth values from D_{raw} as D_{raw}^g , and their depth values from D_{mono} as D_{mono}^g . We then calculate the scale factor a between D_{mono}^g and D_{raw}^g via least squares. We then obtain the regionally aligned depth map D_{mono}^* as:

$$D_{mono}^* = a \cdot D_{mono} + \text{median}(D_{raw}^g). \quad (4)$$

We then fill the missing values in D_{raw} for region g with the corresponding values in the estimated depth map D_{mono}^* . Finally, we perform regional depth-painting for all areas.

3.4 Temporal Stabilization

So far, the model has been treating each frame as separate static scenes. However, this results in significant differences between synthesized novel views for the consecutive frame as shown in Fig. 5. This is because the depth measurements from commodity depth cameras often differ noticeably between frames. Therefore, we propose to condition the neural renderer on both the current frame t and the previous frame $t-1$ to stabilize the novel view video generation process.

One of the approaches is to use optical flow to align feature pixel correspondences across time and warp previous feature images to the current frame to provide the neural renderer with richer information. The results depend heavily on the accuracy of the optical flow estimator [28]. We find in our experiments that the results often have noticeable ghosting artifacts and washed-out object boundaries due to misalignment.

Therefore, we propose to implicitly aggregate information across time without explicit alignment and warping. More specifically, we directly feed the projected feature images F_t and F_{t-1} from frames t and $t-1$ to a GRU-based neural renderer Φ in the reverse time order. We first generate a raw novel view estimation $I_{t,raw}$ and a hidden state Y from the current feature image F_t . Then we generate a refined synthesized novel view estimation I_t given the previous feature image F_{t-1} and hidden state Y_{t-1} . The resulting loss is calculated as:

$$L_{TS} = L(I_{t,raw}, I_{gt}) + L(I_t, I_{gt}). \quad (5)$$

3.5 Cycle Reconstruction Consistency

Although training solely with the baseline loss function gives reasonable results, there are significant ghosting and blurry artifacts. Therefore, we introduce Cycle Reconstruction Consistency (CRC) to reduce these artifacts. The intuition is

that, while there are many ways to generate high-quality novel views close to the ground truth, there are much fewer ways that the generated image can be consistent with other views. Therefore, we require that the model can reproduce the input source images from the synthesized novel view image. In this way, we expect to reduce artifacts that are inconsistent with the input views.

To achieve this, we make the model synthesize the source view image I'_{src} from the novel view image I_{nv} . We render the novel view depth map D_{nv} using the global point cloud. Then our model Φ synthesizes the source image I'_{src} from I_{nv} following the same process described previously in Sec. 3.1. The reconstructed source image is supervised with the same loss function as in Sec. 3.2. This process can be expressed as:

$$I'_{src} = \Phi(D_{nv}, I_{nv}, C_{nv}, C_{src}), \quad (6)$$

$$L_{CRC} = L(I'_{src}, I_{src}). \quad (7)$$

3.6 Combined Loss

We train our model on the combined loss term expressed as follows:

$$L_{combined} = L_{TS} + L_{CRC}. \quad (8)$$

4 Human-Things Interaction (HTI) Dataset

To validate our approach and to support the development of generalizable dynamic view synthesis, we introduce the Human-Things Interaction (HTI) dataset. Compared with previous datasets that only capture the foreground subjects [63,18,19] or static scenes [48,31], our dataset contains diverse interactions between human subjects and their surroundings. Detailed description and samples of the HTI dataset can be found in the supplementary.

Camera Setup Our setup is similar to that of video conferencing and teleconferencing [26,27]. We use two Microsoft Kinect V2 RGBD cameras as source cameras. They capture 1080×1920 RGB videos and 424×512 depth videos at 30 fps, and they are placed 1 to 2 meters in front of the human subjects in an indoor environment. An additional novel view camera is placed in between the source cameras. The cameras are placed 0.4 to 1m apart from each other. Comparing to using a single camera, this setup enables larger range of motion for novel view synthesis and reduces the amount of occlusions. As shown in Fig. 3, we synthesize novel view images using the 2 source cameras on the sides. We use the middle camera to capture ground truth novel view images for supervision during training. We do not use the middle camera during the evaluation.

Capture Process We first calibrate the cameras using a checkerboard pattern and OpenCV[7]. The calibration process outputs estimated intrinsic and distortion parameters for each of the depth and color cameras in the Kinects. Multi-view RGBD videos are then captured with the calibrated source cameras.

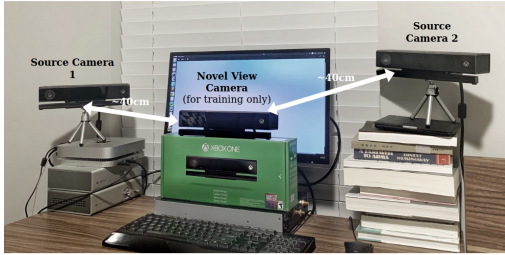


Fig. 3. Our setups involve two source cameras facing towards the scene and an additional novel view camera in the middle that is used only during training.

The resulting videos are synchronized and undistorted. To increase the diversity of the dataset, the relative camera poses and scenes differ between each setup.

Content The dataset includes 43 multi-view RGBD video sequences captured from 12 different camera setups, totaling 77529 RGBD frames from the 3 cameras. It captures one or more people interacting with rigid and deformable objects in 7 different indoor environments. We use 35 sequences captured in 4 different scenes for training and 8 sequences captured in 3 different scenes for evaluation. 1 of the 8 evaluation sequences (sequence 19) contains a known human subject performing *new* actions with a known object in a known environment. The term *known* and *new* refers to the content is previously seen / unseen by the network during training. This sequence is thus used to evaluate the ability of the model to generalize to new actions. The remaining 7 evaluation sequences contain one or more new people performing new actions in new environments. These sequences are used to evaluate the ability of the model to generalize to new human subjects interacting with new objects in new environments.

5 Experiment

In this section, we compare our method against several recent methods. We also perform ablation experiments to investigate the contribution of each proposed component.

5.1 Competing Methods

We compare to the following state-of-the-art methods that are publicly available. The training and inference details of each method are provided in the supplementary material.

FVS [22] FVS is a method that shows good generalizability for static scenes. The original FVS uses depth maps rendered from meshes, which are generated by multi-view stereo software COLMAP[45]. We modify FVS to use the multi-view color videos and fused depth maps instead of meshes. We then generate dynamic free-viewpoint videos by treating each frame as a static scene. We initialize the

Table 1. Comparison between our model and generalizable baselines. Values ordered by PSNR (db) \uparrow / SSIM \uparrow / LPIPS \downarrow . \dagger denotes new actions performed by a known person in a known environment with known objects. All other sequences include new actions performed by a new person/people with new objects in a new environment

	Ours	FVS [41]	RGBD Baseline
seq 19 \dagger	25.910/0.858/0.067	25.346/0.842/0.076	21.419/0.752/0.222
seq 45	25.419/0.827/0.084	23.934/0.777/0.110	21.945/0.710/0.301
seq 49	24.762/0.793/0.091	24.000/0.764/0.115	21.845/0.699/0.304
seq 46	25.240/0.812/0.093	23.563/0.769/0.123	20.004/0.680/0.326
seq 48	23.320/0.790/0.098	22.587/0.766/0.122	20.735/0.669/0.339
seq 47	22.652/0.762/0.116	22.275/0.747/0.135	20.311/0.653/0.357
seq 42	21.046/0.749/0.146	19.477/0.712/0.177	16.804/0.612/0.385
seq 40	20.854/0.735/0.148	18.974/0.696/0.179	17.208/0.575/0.430
all	23.650/0.791/0.105	22.520/0.759/0.130	20.034/0.669/0.333

FVS image encoder and neural renderer with the official pretrained weights and finetune it on our HTI dataset.

RGBD Baseline To understand the benefits of the learning-based methods, we evaluate against an RGBD baseline. This baseline creates colored point clouds from the input RGBD images and then renders them using the same Pytorch3D [40] point cloud renderer as our model.

Non-Generalizable Methods We compare to Neural Scene Flow Fields (NSFF) [22] and DynamicNeRF [15]. Both methods use monocular videos as inputs and require per-video optimization. To make fair comparisons, we modify them to utilize the multi-view RGBD camera inputs as supervision.

Ours To leverage the pretrained weights from static novel view synthesis for the better performance, we adopt the FVS image encoder and neural renderer, and we initialize them with the same pretrained weights as our baseline FVS. We perform neural rendering with point clouds instead of feature-map-warping. Finally, we use the same optimizer settings and batch size as our baseline FVS to finetune our models for the same number of epochs and select the model with the highest performance on the validation sets for the final evaluations.

5.2 Quantitative Comparisons

We evaluate the models on two different generalization settings in Table. 1 and Table. 2. First we evaluate **1) Action generalization**. The given sequence contains known people performing new actions in a known environment with known object (denoted by \dagger in Table. 1 and Table. 2). The term *known* describes contents that have been partially or completely observed in the training data. *new* describes something that is not contained in the training data. For example, in sequence 19 (Fig. 1), the training data contains partial observations of the guitar, and the person wearing the same cloth. But the person is performing a new action of playing guitar. Our model outperforms the baseline FVS by +0.564 dB PSNR, +1.900% SSIM score and -11.842% LPIPS loss (Table. 1). We also

Table 2. Comparison against the non-generalizable models.

	Ours	NSFF [22]	DynamicNeRF [15]
seq 19 †	25.910/0.858/0.067	13.611/0.406/0.512	13.116/0.435/0.475
seq 45	25.419/0.827/0.084	12.996/0.356/0.554	13.775/0.394/0.508
seq 49	24.762/0.793/0.091	13.330/0.329/0.564	12.661/0.356/0.545
all	25.364/0.826/0.080	13.312/0.364/0.543	13.184/0.395/0.509

present a more challenging setting: **2) Complete generalization.** The input sequence contains new people performing new actions in a new environment with new objects. All sequences in Table. 1 and Table. 2, except for sequence 19, correspond to this setting. Our method consistently outperforms the competing methods by healthy margins for all metrics (+1.211 dB PSNR, +4.589% SSIM score, and -19.813% LPIPS loss). However, NSFF and DynamicNeRF fail in both scenarios. Please refer to the supplementary material for more results.



Fig. 4. Qualitative comparisons against FVS on complete generalization (left: seq 45, right: seq 42). Our model shows notable reduction in distortions and ghosting artifacts (*e.g.*, the doors, facial details of the human subjects, and the text on the cardboard). Ours produces more accurate and sharper results (*e.g.*, wrinkles on the man’s shoulder, app icons on the iPad). The proposed Regional Depth-Inpainting module helps increase the completeness of the synthesized images (*e.g.*, the plastic bag).

Table 3. Ablations Study. We use the CRC+RDI+TS model as our final model for the improved temporal consistency and reduced flickering artifacts.

model	PSNR (db) \uparrow /SSIM \uparrow /LPIPS \downarrow
CRC+RDI+TS (Full)	23.650/ 0.791 / 0.105
CRC+RDI	23.777 /0.789/0.108
CRC	23.260/0.789/0.115
FVS baseline	22.520/0.759/0.130

5.3 Qualitative Comparisons

In Fig. 4, we show the comparison against FVS on the complete generalization setting. Our model generates sharper imageries with fewer distortions. Our model more accurately reconstructs the facial details of the human subjects with sharper quality (3rd and 5th column). The text on the cardboard (2nd column) is less distorted and clearer. The icons on the iPad (5th column) are more recognizable. The folds of the clothing (6th column) are better reconstructed for the man in yellow. Moreover, our model significantly reduces ghosting artifacts, as shown by the details of the doors in the second column. Our model also successfully recovers the entire plastic bag (3rd column), which FVS fails to due to missing depth. Additional qualitative comparison results can be found in the supplementary material.

5.4 Ablation Studies

We perform ablation studies on 4 variants of our models to analyze the importance of each module. They are: (1) "FVS baseline", which is the finetuned FVS model, (2) "CRC", where Cycle Reconstruction Consistency and feature point clouds are used, (3) "CRC+RDI", where Regional Depth-Inpainting (RDI) is used in addition to CRC, (4) and "CRC+RDI+TS (Full)", our full model where Temporal Stabilization is used as well. RDI is only applied during the test time for all variants, which we find to improve the performance. In Table. 3, We show the performance of each variant averaged over all test frames. As demonstrated by the "CRC" and "CRC+RDI" entries, both CRC and RDI provide the notable improvements to the performance. While our full model (CRC+RDI+TS) and CRC+RDI are very close in terms of average quantitative performance, qualitative ablations show that our full model notably increases the temporal stability. As shown in Fig. 5-(b), we are able to reduce flickering artifacts via the Temporal Stabilization (TS) module. Moreover, the Temporal Stabilization module improves the view synthesis quality (e.g. the label on the box and the text below it in Fig. 5-(a)).

6 Limitations

The main limitation of our approach is the reliance on accurate depth measurements. Although we can notably improve upon the baselines, our results still

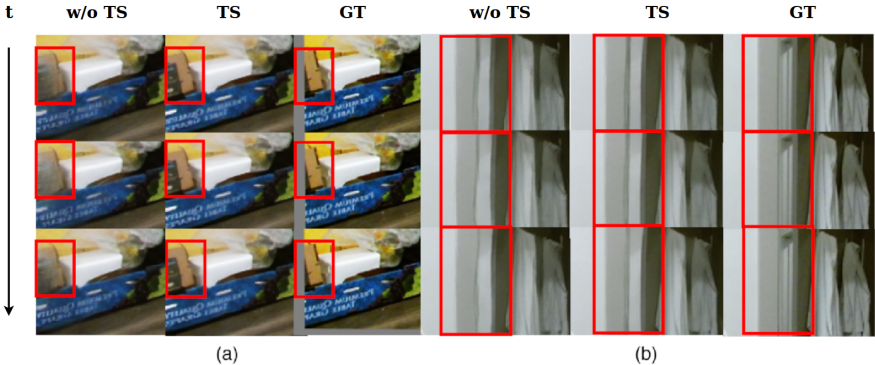


Fig. 5. Visualization of the effect of Temporal Stabilization (TS) module, tested on (a) sequence 19 (action generalization setting) and (b) sequence 46 (complete generalization setting). Our Temporal Stabilization module provides noticeably better temporal stability and distortion reduction (*e.g.*, the door frame in (b)) even though the depth inputs are unstable and inaccurate. Moreover, TS enables the model to recover details that would have been lost if only the current frame is utilized as seen in (a). The gray borders in the groundtruth images are due to camera undistortion.

show significant flickering due to low-fidelity RGBD cameras, *i.e.*, the \$40 Kinect V2 cameras. Possible solutions include (1) utilizing better RGBD cameras (*e.g.*, Azure Kinect). (2) simple background pre-scanning. (3) depth refinement using visual observations. It is also valuable to improve the speed and thus enable real-time novel view synthesis, which would pave the way to our end goal, *i.e.*, commodity telepresence systems. We leave these items for future development.

7 Conclusions

This paper presents a dynamic novel view synthesis system that utilizes a few commodity RGBD cameras to synthesize free-viewpoint videos for challenging dynamic scenes. Our work does not require per-scene optimization, prior models, or expensive preprocessing. The core challenge lies in the artifacts induced by inaccurate, unstable, and incomplete depth inputs from the RGBD cameras. We enforce spatial-temporal consistency of the view synthesis process via the proposed Cycle Reconstruction Consistency and Temporal Stabilization modules to reduce these artifacts. We also developed a simple Regional Depth-Inpainting module to compensate for incomplete depth input. Finally, we collected the Human-Things Interactions (HTI) dataset to train and validate our approach. Quantitative and qualitative evaluations show that our model can synthesize free-viewpoint videos of dynamic scenes with increased stability and fidelity compared to the baseline FVS[41]. We intend to improve both the speed and visual quality to enable real-time telepresence systems with commodity RGBD cameras for future work.

References

1. Alex Yu and Sara Fridovich-Keil, Tancik, M., Chen, Q., Recht, B., Kanazawa, A.: Plenoxels: Radiance fields without neural networks (2021)
2. Aliev, K.A., Sevastopolsky, A., Kolos, M., Ulyanov, D., Lempitsky, V.: Neural point-based graphics (2020)
3. Attal, B., Laidlaw, E., Gokaslan, A., Kim, C., Richardt, C., Tompkin, J., O’Toole, M.: Törf: Time-of-flight radiance fields for dynamic scene view synthesis. *Advances in Neural Information Processing Systems* **34** (2021)
4. Attal, B., Ling, S., Gokaslan, A., Richardt, C., Tompkin, J.: Matryodshka: Real-time 6dof video view synthesis using multi-sphere images. *CoRR* **abs/2008.06534** (2020), <https://arxiv.org/abs/2008.06534>
5. Barron, J.T., Mildenhall, B., Tancik, M., Hedman, P., Martin-Brualla, R., Srinivasan, P.P.: Mip-nerf: A multiscale representation for anti-aliasing neural radiance fields (2021)
6. Bozic, A., Zollhöfer, M., Theobalt, C., Nießner, M.: Deepdeform: Learning non-rigid RGB-D reconstruction with semi-supervised data. *CoRR* **abs/1912.04302** (2019), <http://arxiv.org/abs/1912.04302>
7. Bradski, G.: The OpenCV Library. *Dr. Dobb’s Journal of Software Tools* (2000)
8. Broxton, M., Flynn, J., Overbeck, R., Erickson, D., Hedman, P., DuVall, M., Dourgarian, J., Busch, J., Whalen, M., Debevec, P.: Immersive light field video with a layered mesh representation **39**(4), 86:1–86:15 (2020)
9. Chang, W.: Holoportation: Virtual 3d teleportation in real-time (March 2016), <https://www.microsoft.com/en-us/research/publication/holoportation-virtual-3d-teleportation-in-real-time/>
10. Chen, A., Xu, Z., Zhao, F., Zhang, X., Xiang, F., Yu, J., Su, H.: Mvsnerf: Fast generalizable radiance field reconstruction from multi-view stereo. *arXiv preprint arXiv:2103.15595* (2021)
11. Chen, Q., Koltun, V.: Photographic image synthesis with cascaded refinement networks. *CoRR* **abs/1707.09405** (2017), <http://arxiv.org/abs/1707.09405>
12. Chibane, J., Bansal, A., Lazova, V., Pons-Moll, G.: Stereo radiance fields (srf): Learning view synthesis from sparse views of novel scenes. In: *IEEE Conference on Computer Vision and Pattern Recognition (CVPR)*. IEEE (jun 2021)
13. Deng, K., Liu, A., Zhu, J.Y., Ramanan, D.: Depth-supervised nerf: Fewer views and faster training for free. *arXiv preprint arXiv:2107.02791* (2021)
14. Dou, M., Davidson, P., Fanello, S.R., Khamis, S., Kowdle, A., Rhemann, C., Tankovich, V., Izadi, S.: Motion2fusion: real-time volumetric performance capture. In: *ACM SIGGRAPH Conference on Computer Graphics and Interactive Techniques* (2017)
15. Gao, C., Saraf, A., Kopf, J., Huang, J.: Dynamic view synthesis from dynamic monocular video. *CoRR* **abs/2105.06468** (2021), <https://arxiv.org/abs/2105.06468>
16. Garbin, S.J., Kowalski, M., Johnson, M., Shotton, J., Valentin, J.: Fastnerf: High-fidelity neural rendering at 200fps. *arXiv preprint arXiv:2103.10380* (2021)
17. Hedman, P., Srinivasan, P.P., Mildenhall, B., Barron, J.T., Debevec, P.: Baking neural radiance fields for real-time view synthesis. *ICCV* (2021)
18. Ionescu, C., Papava, D., Olaru, V., Sminchisescu, C.: Human3.6m: Large scale datasets and predictive methods for 3d human sensing in natural environments. *IEEE Transactions on Pattern Analysis and Machine Intelligence* **36**(7), 1325–1339 (jul 2014)

19. Joo, H., Simon, T., Li, X., Liu, H., Tan, L., Gui, L., Banerjee, S., Godisart, T.S., Nabbe, B., Matthews, I., Kanade, T., Nobuhara, S., Sheikh, Y.: Panoptic studio: A massively multiview system for social interaction capture. *IEEE Transactions on Pattern Analysis and Machine Intelligence* (2017)
20. Kopanas, G., Philip, J., Leimkühler, T., Drettakis, G.: Point-based neural rendering with per-view optimization. *CoRR* **abs/2109.02369** (2021), <https://arxiv.org/abs/2109.02369>
21. Kwon, Y., Kim, D., Ceylan, D., Fuchs, H.: Neural human performer: Learning generalizable radiance fields for human performance rendering. *Advances in Neural Information Processing Systems* **34** (2021)
22. Li, Z., Niklaus, S., Snavely, N., Wang, O.: Neural scene flow fields for space-time view synthesis of dynamic scenes. In: *Proceedings of the IEEE/CVF Conference on Computer Vision and Pattern Recognition (CVPR)* (2021)
23. Lindell, D.B., Martel, J.N.P., Wetzstein, G.: Autoint: Automatic integration for fast neural volume rendering. In: *Proc. CVPR* (2021)
24. Liu, L., Habermann, M., Rudnev, V., Sarkar, K., Gu, J., Theobalt, C.: Neural actor: Neural free-view synthesis of human actors with pose control. *ACM Trans. Graph.(ACM SIGGRAPH Asia)* (2021)
25. Loper, M., Mahmood, N., Romero, J., Pons-Moll, G., Black, M.J.: SMPL: A skinned multi-person linear model. *ACM Trans. Graphics (Proc. SIGGRAPH Asia)* **34**(6), 248:1–248:16 (Oct 2015)
26. Maimone, A., Fuchs, H.: Encumbrance-free telepresence system with real-time 3d capture and display using commodity depth cameras. In: *2011 10th IEEE International Symposium on Mixed and Augmented Reality*. pp. 137–146 (2011). <https://doi.org/10.1109/ISMAR.2011.6092379>
27. Maimone, A., Yang, X., Dierk, N., State, A., Dou, M., Fuchs, H.: General-purpose telepresence with head-worn optical see-through displays and projector-based lighting. In: *2013 IEEE Virtual Reality (VR)*. pp. 23–26 (2013). <https://doi.org/10.1109/VR.2013.6549352>
28. Martin-Brualla, R., Pandey, R., Yang, S., Pidlypenskyi, P., Taylor, J., Valentin, J.P.C., Khamis, S., Davidson, P.L., Tkach, A., Lincoln, P., Kowdle, A., Rhemann, C., Goldman, D.B., Keskin, C., Seitz, S.M., Izadi, S., Fanello, S.R.: Lookingood: Enhancing performance capture with real-time neural re-rendering. *CoRR* **abs/1811.05029** (2018), <http://arxiv.org/abs/1811.05029>
29. Mildenhall, B., Srinivasan, P.P., Tancik, M., Barron, J.T., Ramamoorthi, R., Ng, R.: Nerf: Representing scenes as neural radiance fields for view synthesis. In: *European conference on computer vision*. pp. 405–421. Springer (2020)
30. Müller, T., Evans, A., Schied, C., Keller, A.: Instant neural graphics primitives with a multiresolution hash encoding. *arXiv:2201.05989* (Jan 2022)
31. Nathan Silberman, Derek Hoiem, P.K., Fergus, R.: Indoor segmentation and support inference from rgbd images. In: *ECCV* (2012)
32. Newcombe, R.A., Fox, D., Seitz, S.M.: Dynamicfusion: Reconstruction and tracking of non-rigid scenes in real-time. In: *Proceedings of the IEEE Conference on Computer Vision and Pattern Recognition (CVPR)* (June 2015)
33. Nguyen, P., Sarafianos, N., Lassner, C., Heikkilä, J., Tung, T.: Human view synthesis using a single sparse rgb-d input (2021)
34. Osman, A.A.A., Bolkart, T., Black, M.J.: STAR: A sparse trained articulated human body regressor. In: *European Conference on Computer Vision (ECCV)*. pp. 598–613 (2020), <https://star.is.tue.mpg.de>
35. Park, K., Sinha, U., Barron, J.T., Bouaziz, S., Goldman, D.B., Seitz, S.M., Martin-Brualla, R.: Nerfies: Deformable neural radiance fields. *ICCV* (2021)

36. Park, K., Sinha, U., Hedman, P., Barron, J.T., Bouaziz, S., Goldman, D.B., Martin-Brualla, R., Seitz, S.M.: Hypernerf: A higher-dimensional representation for topologically varying neural radiance fields. *ACM Trans. Graph.* **40**(6) (dec 2021)
37. Peng, S., Dong, J., Wang, Q., Zhang, S., Shuai, Q., Zhou, X., Bao, H.: Animatable neural radiance fields for modeling dynamic human bodies. In: *ICCV* (2021)
38. Peng, S., Zhang, Y., Xu, Y., Wang, Q., Shuai, Q., Bao, H., Zhou, X.: Neural body: Implicit neural representations with structured latent codes for novel view synthesis of dynamic humans. In: *CVPR* (2021)
39. Ranftl, R., Bochkovskiy, A., Koltun, V.: Vision transformers for dense prediction. *ArXiv preprint* (2021)
40. Ravi, N., Reizenstein, J., Novotny, D., Gordon, T., Lo, W.Y., Johnson, J., Gkioxari, G.: Accelerating 3d deep learning with pytorch3d. *arXiv:2007.08501* (2020)
41. Riegler, G., Koltun, V.: Free view synthesis. *CoRR* **abs/2008.05511** (2020), <https://arxiv.org/abs/2008.05511>
42. Riegler, G., Koltun, V.: Stable view synthesis. In: *Proceedings of the IEEE/CVF Conference on Computer Vision and Pattern Recognition*. pp. 12216–12225 (2021)
43. Ronneberger, O., Fischer, P., Brox, T.: U-net: Convolutional networks for biomedical image segmentation. In: *International Conference on Medical image computing and computer-assisted intervention*. pp. 234–241. Springer (2015)
44. Rückert, D., Franke, L., Stamminger, M.: Adop: Approximate differentiable one-pixel point rendering. *arXiv preprint arXiv:2110.06635* (2021)
45. Schönberger, J.L., Zheng, E., Pollefeys, M., Frahm, J.M.: Pixelwise view selection for unstructured multi-view stereo. In: *European Conference on Computer Vision (ECCV)* (2016)
46. Simonyan, K., Zisserman, A.: Very deep convolutional networks for large-scale image recognition. *arXiv preprint arXiv:1409.1556* (2014)
47. Sitzmann, V., Martel, J.N., Bergman, A.W., Lindell, D.B., Wetzstein, G.: Implicit neural representations with periodic activation functions. In: *arXiv* (2020)
48. Song, S., Lichtenberg, S.P., Xiao, J.: Sun rgb-d: A rgb-d scene understanding benchmark suite. In: *2015 IEEE Conference on Computer Vision and Pattern Recognition (CVPR)*. pp. 567–576 (2015). <https://doi.org/10.1109/CVPR.2015.7298655>
49. Srinivasan, P.P., Tucker, R., Barron, J.T., Ramamoorthi, R., Ng, R., Snavely, N.: Pushing the boundaries of view extrapolation with multiplane images. In: *Proceedings of the IEEE/CVF Conference on Computer Vision and Pattern Recognition*. pp. 175–184 (2019)
50. Su, S.Y., Yu, F., Zollhöfer, M., Rhodin, H.: A-nerf: Articulated neural radiance fields for learning human shape, appearance, and pose. In: *Advances in Neural Information Processing Systems* (2021)
51. Szeliski, R., Golland, P.: Stereo matching with transparency and matting. In: *Sixth International Conference on Computer Vision (IEEE Cat. No. 98CH36271)*. pp. 517–524. IEEE (1998)
52. Tancik, M., Srinivasan, P.P., Mildenhall, B., Fridovich-Keil, S., Raghavan, N., Singhal, U., Ramamoorthi, R., Barron, J.T., Ng, R.: Fourier features let networks learn high frequency functions in low dimensional domains. *NeurIPS* (2020)
53. Tretschk, E., Tewari, A., Golyanik, V., Zollhöfer, M., Lassner, C., Theobalt, C.: Non-rigid neural radiance fields: Reconstruction and novel view synthesis of a dynamic scene from monocular video. In: *IEEE International Conference on Computer Vision (ICCV)*. IEEE (2021)
54. Tucker, R., Snavely, N.: Single-view view synthesis with multiplane images. In: *The IEEE Conference on Computer Vision and Pattern Recognition (CVPR)* (June 2020)

55. Wang, J., Nie, X., Xia, Y., Wu, Y., Zhu, S.: Cross-view action modeling, learning and recognition. CoRR **abs/1405.2941** (2014), <http://arxiv.org/abs/1405.2941>
56. Wang, Q., Wang, Z., Genova, K., Srinivasan, P., Zhou, H., Barron, J.T., Martin-Brualla, R., Snavely, N., Funkhouser, T.: Ibrnet: Learning multi-view image-based rendering. In: CVPR (2021)
57. Wiles, O., Gkioxari, G., Szeliski, R., Johnson, J.: SynSin: End-to-end view synthesis from a single image. In: CVPR (2020)
58. Xian, W., Huang, J.B., Kopf, J., Kim, C.: Space-time neural irradiance fields for free-viewpoint video. In: Proceedings of the IEEE/CVF Conference on Computer Vision and Pattern Recognition (CVPR). pp. 9421–9431 (2021)
59. Yoon, J.S., Kim, K., Gallo, O., Park, H.S., Kautz, J.: Novel view synthesis of dynamic scenes with globally coherent depths from a monocular camera. In: Proceedings of the IEEE/CVF Conference on Computer Vision and Pattern Recognition. pp. 5336–5345 (2020)
60. Yu, A., Li, R., Tancik, M., Li, H., Ng, R., Kanazawa, A.: PlenOctrees for real-time rendering of neural radiance fields. In: ICCV (2021)
61. Yu, A., Ye, V., Tancik, M., Kanazawa, A.: pixelnerf: Neural radiance fields from one or few images (2020)
62. Zhang, K., Riegler, G., Snavely, N., Koltun, V.: Nerf++: Analyzing and improving neural radiance fields. CoRR **abs/2010.07492** (2020), <https://arxiv.org/abs/2010.07492>
63. Zheng, Z., Yu, T., Wei, Y., Dai, Q., Liu, Y.: Deephuman: 3d human reconstruction from a single image. In: The IEEE International Conference on Computer Vision (ICCV) (October 2019)
64. Zhou, T., Tucker, R., Flynn, J., Fyffe, G., Snavely, N.: Stereo magnification: Learning view synthesis using multiplane images. In: SIGGRAPH (2018)
65. Zollhöfer, M., Nießner, M., Izadi, S., Rhemann, C., Zach, C., Fisher, M., Wu, C., Fitzgibbon, A., Loop, C., Theobalt, C., Stamminger, M.: Real-time non-rigid reconstruction using an rgb-d camera. ACM Transactions on Graphics (TOG) **33**(4) (2014)

8 Human-Things Interaction Dataset

Human-Things Interaction (HTI) dataset captures interactions between human subjects and objects in indoor environments. In *dataset_visualization.mp4*, we visualize some of the sequences used for training and evaluation. Each sequence is around 20 seconds and consists of calibrated and synchronized multi-view RGBD inputs. Almost all of the sequences in the training set contains the same male as the human subject, although he appears in different outfits. One additional female subject appears in some sequences. All the test sequences contain one or more male or female subjects (except for sequence 19 where the same male subject in the training set).

9 Video results

In the supplementary video *visual_comparisons.mp4*, we show video comparisons between the baseline Free View Synthesis [41], our model, NSFF[22], and DynamicNeRF[15]. We also show significantly more stable results when using Microsoft Azure Kinect RGBD cameras instead of Kinect V2 cameras. Finally, we also provide video visualizations of our HTI dataset used for training and testing.

10 Training and Evaluation details

Ours and FVS [41] We use the same training settings of the original Free View Synthesis (FVS) [41] for both the FVS baseline and our model. More specifically, we train both FVS and our model using the ADAM optimizer with a learning rate of 10^{-4} , $\beta_1 = 0.9$, $\beta_2 = 0.9999$, and $\epsilon = 10^{-8}$. We finetune both models on our HTI dataset for five epochs (*i.e.*, 13005 iterations in total) with a batch size of 4 on 4 NVIDIA GeForce RTX 3090 GPUs. For the final evaluation, we choose the weights of each model from the epoch with the highest validation performance.

Per-Scene Optimized Methods We compare to Neural Scene Flow Fields (NSFF) [22] and DynamicNeRF [15]. Since both models originally use monocular RGB videos as inputs, we modified them to use the 2 RGBD frames available at each timestamp to ensure fair comparisons. The depth frames are the rendering of the global point cloud instead of the raw depth images from the Kinect V2 cameras. They are thus more complete and more suitable to be used as supervisions. As suggested by the authors of NSFF [22] on Github, the default NSFF performs the best when trained on 30-60 frame videos. Therefore, we train NSFF and DynamicNeRF on 30-frame clips extracted from the 8 test sequences in our dataset. We train both models with default parameters. However, we use 1792 (instead of the default 1024) ray samples on each GPU for faster convergence. We train the models on 4 NVIDIA GeForce RTX 3090 (*i.e.* 7168 total ray samples each iteration) for 200k iterations and confirm that the models have converged. For evaluation, we render images from the ground truth novel viewpoint and compare them to the ground truth novel view frames.

11 Comparisons to NeRF-Based Methods

In this section, we compare our full model to Neural Scene Flow Fields (NSFF) [22] and DynamicNeRF [15]. As shown in Table. 4, we outperform both the NSFF and DynamicNeRF on every sequence and every metric by a large margin. This is because both methods fail to learn the geometry of the scenes, as shown in Fig. 6. We conjecture that this is because of our sparse fixed cameras instead of moving cameras used in the original works. Both DynamicNeRF and NSFF are able to gather multi-view information about the scene via moving monocular cameras. The access to multi-view information thus allows the radiance fields to resolve ambiguities and avoid degenerate solutions as shown here. Please refer to our supplementary video *visual_comparisons.mp4* for renderings from both models.

We are also aware of TöRF [3] which is very related to our work since it can process Time-of-Flight and depth inputs for dynamic scenes. However, due to limited computational resources, we only compared to NSFF and DynamicNeRF.



Fig. 6. Both DynamicNeRF[15] and NSFF[22] fail to reconstruct the scenes.

12 Regional Depth-Inpainting

In this section, we provide visualizations for the Regional Depth-Inpainting module. As shown in Fig. 7, we first extract regions of missing depth values via morphologically filtering the depth map. The different colors denote different regions that would later receive different alignment parameters. The darkest regions are the regions where the depth pixels are deemed to be valid. Each region is then expanded to increase the overlap between the raw depth maps (*i.e.*, depth renderings of the global point clouds) and the depth maps estimated by the monocular

Table 4. Comparison against NSFF[22] and DynamicNeRF[15]. Values ordered by PSNR (db) \uparrow / SSIM \uparrow / LPIPS \downarrow . "N/A" denotes evaluations that are skipped.

	Ours	NSFF [22]	DynamicNeRF [15]
seq 19 †	25.910/0.858/0.067	13.611/0.406/0.512	13.116/0.435/0.475
seq 45	25.419/0.827/0.084	12.996/0.356/0.554	13.775/0.394/0.508
seq 49	24.762/0.793/0.091	13.330/0.329/0.564	12.661/0.356/0.545
seq 46	25.240/0.812/0.093	N/A	12.464/0.309/0.540
seq 48	23.320/0.790/0.098	N/A	12.388/0.343/0.525
seq 47	22.652/0.762/0.116	N/A	13.526/0.356/0.517
seq 42	21.046/0.749/0.146	N/A	12.297/0.341/0.528
seq 40	20.854/0.735/0.148	N/A	12.055/0.340/0.526
all	23.650/0.791/0.105	N/A	12.785/0.359/0.521

depth estimator, MiDaS [39]. We then use the overlapping pixels of each region and the raw depth map to calculate its alignment. In Fig. 7, the wrongly in-painted depth values in the red circles demonstrate that naive alignment of the entire depth maps result in misalignment and thus artifacts in the synthesized novel views. However, the locally aligned depth maps are effective in avoiding such artifacts while completing the depth maps.



Fig. 7. Regional Depth-Inpainting is able to reduce the amount of misalignment and thus reduce the artifacts in the final rendering

13 More Visual Results

We provide more comparison results with FVS on the *complete generalization* setting in Fig. 8 and video *seq_49_comparison.avi*. As shown in all figures, our model achieves notably less distortion and more accurate reconstructions comparing to the FVS baseline.



Fig. 8. Our model achieves higher quality rendering and reduced distortions

13.1 Evaluation on Azure Kinect Cameras

We also evaluated our model on its ability to generalize to new cameras. Different cameras exhibit different characteristics *e.g.* noise distributions, distortion, RGB-to-Depth misalignment, etc. The videos shown in Fig. 9 are captured with Microsoft Azure Kinect RGBD cameras. Our model notably reduce amount of distortions despite the use of cameras different from the training set. However, the baseline FVS suffers from heavy distortions and ghosting artifacts. Moreover, as shown in our supplementary videos *seq_multi_azure_ktulu_3_comparison.avi* and *seq_multi_azure_ktulu_4_comparison.avi*, our model is notably more stable than the FVS baseline when using Azure Kinect cameras instead of Kinect V2 cameras. This is likely because Azure Kinect cameras are notably more stable, complete, and cleaner than that of the Kinect V2 cameras. The difference in stability is more pronounced with Azure Kinect cameras than Kinect V2 cameras. Therefore, we conjecture that our model benefits more from stable depth measurements than the baseline FVS. However, we notice that the results from Azure Kinect are blurry in general, and the dynamic contents (*e.g.* human) are less accurate than the results from Kinect V2. We suspect that this is because we performed custom calibrations for Kinect V2 cameras, but we used default calibration and distortion parameters provided by the manufacturer for Azure Kinect cameras.

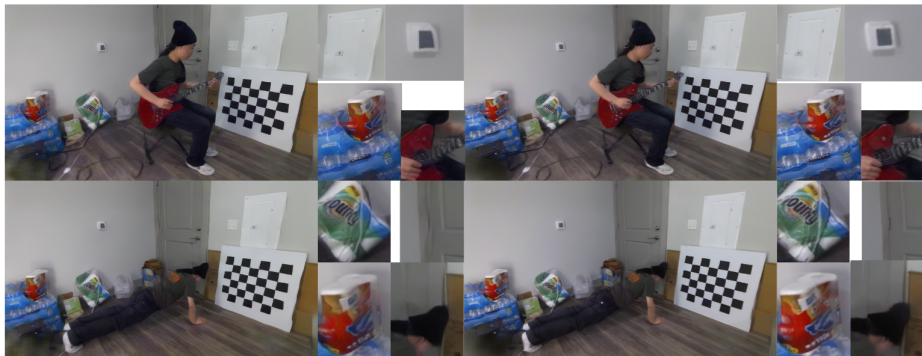


Fig. 9. The improvement in performance is more pronounced when Azure Kinect cameras are used. Please see the supplementary videos for better visualization of temporal stability.